coatings

MDPI

Article

Ta–Zr–N Thin Films Fabricated through HIPIMS/RFMS Co-Sputtering

Li-Chun Chang [1,2,*], Ching-Yen Chang [1] and Ya-Wen You [1]

[1] Department of Materials Engineering, Ming Chi University of Technology, New Taipei City 24301, Taiwan; a22910936@yahoo.com.tw (C.-Y.C.); tank95173@gmail.com (Y.-W.Y.)

[2] Center for Thin Film Technologies and Applications, Ming Chi University of Technology, New Taipei City 24301, Taiwan

* Correspondence: lcchang@mail.mcut.edu.tw; Tel.: +886-2-2908-9899

Academic Editor: Pascal Briois

Received: 31 August 2017; Accepted: 2 November 2017; Published: 4 November 2017

Abstract: Ta–Zr–N thin films were fabricated through co-deposition of radio-frequency magnetron sputtering and high-power impulse magnetron sputtering (HIPIMS/RFMS co-sputtering). The oxidation resistance of the fabricated films was evaluated by annealing the samples in a 15-ppm O_2-N_2 atmosphere at 600 °C for 4 and 8 h. The mechanical properties and surface roughness of the as-deposited and annealed thin films were evaluated. The results indicated that the HIPIMS/RFMS co-sputtered Ta–Zr–N thin films exhibited superior mechanical properties and lower surface roughness than did the conventional direct current-sputtered Ta–Zr–N thin films and HIPIMS-fabricated ZrN_x thin films in both the as-deposited and annealed states.

Keywords: annealing; HIPIMS; mechanical properties; oxidation resistance

1. Introduction

Ta–Zr–N coatings have been employed as protective coatings against wear for biomedical implants [1,2] and as diffusion barrier layers in Cu metallization [3]. Ta-rich Ta–Zr–N coatings exhibited enhanced toughness with high hardness [4,5]. In a previous study [6], low-Zr-content $Ta_{1-x}Zr_xN_y$ thin films (x = 0–0.17, y = 0.86–1.03) fabricated through conventional reactive direct-current (DC) magnetron co-sputtering exhibited desirable mechanical properties and a restricted increase in surface roughness from 0.9–1.5 nm to 1.2–1.7 nm after annealing at 600 °C in a 15-ppm O_2-N_2 atmosphere for 4 h. The chemical inertness of these films against commercial moldable SiO_2–B_2O_3–BaO-based glass after 500 thermal cycles was experimentally confirmed. Thermal cycling annealing at 270 °C and 600 °C in a 15-ppm O_2-N_2 atmosphere was a realistic mass production process [7,8]. The smoothing mechanism of coating surfaces is a crucial factor when Ta–Zr–N thin films are deposited as the protective coatings on glass molding dies. High-power pulsed magnetron sputtering (also called high-power impulse magnetron sputtering (HIPIMS) [9,10]) has broadened the operating window of magnetron sputtering. HIPIMS was proposed as a method for growing high-quality films with dense structure, smooth morphology, and excellent adhesion [11], and has attracted substantial industry and research interest because of its potential use in such applications as wear resistance [11,12] and electric coatings [13]. However, despite its superiority, the mechanism underlying HIPIMS is complex because many factors—particularly pulse parameters—affect the deposition process. The low deposition rate in the HIPIMS process became a drawback for the commercial applications [10,14]. Therefore, hybrid processes, such as HIPIMS/DCMS (direct-current magnetron co-sputtering) [15] and HIPIMS/AIP (arc ion plating) [16] were utilized. In this study, co-deposition of radio-frequency magnetron sputtering and HIPIMS (hereafter, HIPIMS/RFMS co-sputtering) was used to improve the

surface quality (decrease the surface roughness) of Ta–Zr–N thin films, and its effects on the mechanical properties and oxidation resistance of the films were investigated.

2. Materials and Methods

An HIPIMS/RFMS co-sputtering system (Figure 1) was employed to deposit Ta–Zr–N thin films on silicon substrates. A 99.95% pure Ta target was connected to an RF power generator (13.56 MHz), and a 99.9% pure Zr target was connected to a SPIK2000A pulse power supply (SPIK 2000A; Shen Chang Electric Co., Taipei, Taiwan) operated in the unipolar negative mode at a constant power of 400 W. Both targets were 76.2 mm in diameter, and tilted to the vertical axis. The pulse on-time, t_{on}, and pulse off-time, t_{off}, were kept constant at 100 and 3900 μs, respectively. The duty cycle ($t_{on}/(t_{off} + t_{on}) \times 100\%$) was maintained at 2.5%. The substrate-to-target vertical distance was 12 cm, and the chamber was pumped to a base pressure of 6.7×10^{-4} Pa. The working pressure was maintained at approximately 0.67 Pa by flowing an Ar and N_2 (Ar:N_2 = 9:1) gas mixture into the chamber. The substrate holder was rotated at 10 rpm during the process. A pulse bias voltage of −50 V was applied to the substrate holder, and the coatings were deposited at 400 °C. Table 1 lists the sputtering powers employed to fabricate the Ta–Zr–N thin films; the deposition times were altered to achieve coating thicknesses of 1217–1279 nm. The Ta–Zr–N thin films were further annealed at 600 °C for 4 and 8 h in a 15-ppm O_2-N_2 atmosphere in a quartz tube furnace.

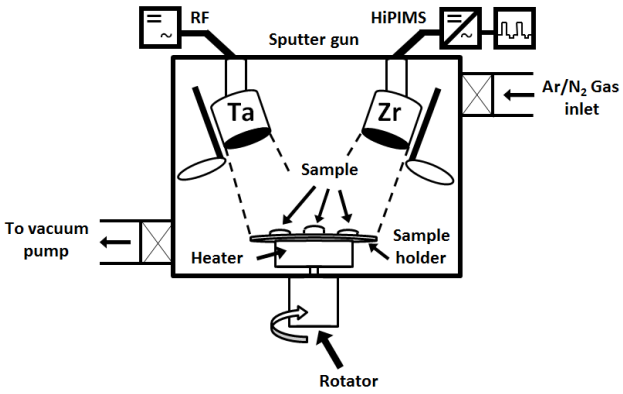

Figure 1. Schematic image of the radio-frequency magnetron sputtering and high-power impulse magnetron sputtering (HIPIMS/RFMS) co-sputtering equipment.

Table 1. Sputter parameters for depositing Ta–Zr–N thin films.

Sample	RF Power W_{Ta}	HIPIMS Power W_{Zr}	Zr Power Density (W/cm^2)	Deposition Time (min)	Coating Thickness (nm)	Deposition Rate (nm/min)
A	100	400	1656	210	1217	5.80
B	200	400	1632	140	1238	8.84
C	300	400	1576	105	1279	12.18
D	400	400	1500	85	1253	14.75

Chemical composition analysis was conducted by using a field-emission electron probe microanalyzer (FE-EPMA, JXA-8500F, JEOL, Akishima, Japan) on the surface of the samples. The film and oxide scale thicknesses were evaluated by field emission scanning electron microscopy (FE-SEM, S4800, Hitachi, Tokyo, Japan) on the fracture surface of the samples, initiated from the backside of Si wafers. A conventional X-ray diffractometer (XRD, X'Pert PRO MPD, PANalytical, Almelo, The Netherlands) with Cu Kα radiation was adopted to identify the phases of the coatings, using the grazing incidence technique with an incidence angle of 1°. The nanostructure of the coatings and scales was further examined using transmission electron microscopy (TEM, JEM-2010F, JEOL, Akishima, Japan) at a 200-kV accelerating voltage. TEM samples were prepared by applying a focused ion beam system (FEI Nova 200, Hillsboro, OR, USA) at an accelerating voltage of 30 kV with a gallium ion

source. A Pt layer was deposited to protect the free surface during sample preparation. The surface nanoindentation hardness values of $Ta_{1-x}Zr_xN_y$ coatings were measured with a nanoindentation tester (TI-900 Triboindenter, Hysitron, Eden Prairie, MN, USA). The nanoindenter was equipped with a Berkovich diamond probe tip. The applied load was controlled to exhibit an indentation depth of 100 nm. The loading, holding, and unloading times were 5 s each. The nanoindentation hardness and reduced elastic modulus E_r of each indent were calculated based on the Oliver and Pharr method [17]. The elastic modulus, E, of a film can be determined from:

$$\frac{1}{E_r} = \frac{1-\nu^2}{E} + \frac{1-\nu_i^2}{E_i} \quad (1)$$

where E, ν, E_i, and ν_i are the elastic modulus and Poisson's ratio of the film and indenter, using ν = 0.25, E_i = 1141 GPa, and ν_i = 0.07 [18], respectively. The surface roughness values of the coatings were evaluated by using an atomic force microscope (AFM, Dimension 3100 SPM, NanoScope IIIa, Veeco, New York, NY, USA). The scanning area of each image was set at 5 μm × 5 μm with a scanning rate of 1.0 Hz. The residual stress of the films measured by the curvature method was calculated using Stoney's equation [19].

3. Results and Discussion

3.1. As-Deposited Ta–Zr–N Thin Films

Table 2 lists the elemental compositions of the as-deposited Ta–Zr–N thin films prepared through HIPIMS/RFMS co-sputtering. The Ta content in the Ta–Zr–N thin films increased with increasing Ta target power. The oxygen content in the as-deposited states were 1.0–2.3 at %. The samples were designated in the form $Ta_{1-x}Zr_xN_y$, as follows: $Ta_{0.84}Zr_{0.16}N_{0.40}$, $Ta_{0.81}Zr_{0.19}N_{0.52}$, $Ta_{0.58}Zr_{0.42}N_{0.59}$, and $Ta_{0.33}Zr_{0.67}N_{0.68}$. The atomic ratio of N/(Ta + Zr) increased from 0.40 to 0.52, 0.59, and 0.68 as the power of the Ta target increased from 100 to 200, 300, and 400 W, respectively. The deposition parameters were adjusted to fabricate thin films of similar thicknesses (Table 1); the $Ta_{0.84}Zr_{0.16}N_{0.40}$, $Ta_{0.81}Zr_{0.19}N_{0.52}$, $Ta_{0.58}Zr_{0.42}N_{0.59}$, and $Ta_{0.33}Zr_{0.67}N_{0.68}$ thin films were 1253, 1279, 1238, and 1217 nm thick, respectively.

Table 2. Chemical compositions of as-deposited and 600 °C-annealed Ta–Zr–N thin films.

Sample	Annealing Time (*h*)	Chemical Composition (at %)				Atomic Ratio	
		Ta	Zr	N	O	Zr/(Ta + Zr)	N/(Ta + Zr)
A $Ta_{0.33}Zr_{0.67}N_{0.68}$	0	19.0 ± 0.0	39.1 ± 0.5	39.6 ± 0.2	2.3 ± 0.2	0.67	0.68
	4	17.5 ± 0.4	35.9 ± 0.3	34.0 ± 0.7	12.6 ± 1.0	0.67	0.64
	8	16.3 ± 0.4	33.6 ± 0.5	30.9 ± 0.3	19.2 ± 1.3	0.67	0.62
B $Ta_{0.58}Zr_{0.42}N_{0.59}$	0	36.3 ± 0.1	26.1 ± 0.2	36.6 ± 0.1	1.0 ± 0.0	0.42	0.59
	4	29.3 ± 0.5	23.0 ± 0.8	28.2 ± 0.5	19.5 ± 1.5	0.44	0.54
	8	27.5 ± 0.5	21.8 ± 0.1	26.8 ± 0.3	23.9 ± 0.3	0.44	0.54
C $Ta_{0.81}Zr_{0.19}N_{0.52}$	0	52.5 ± 0.2	12.5 ± 0.7	33.5 ± 0.2	1.5 ± 0.3	0.19	0.52
	4	35.8 ± 0.4	16.1 ± 0.4	24.1 ± 0.0	24.0 ± 0.3	0.31	0.46
	8	33.0 ± 0.3	14.9 ± 0.3	22.7 ± 0.3	29.4 ± 0.3	0.31	0.47
D $Ta_{0.84}Zr_{0.16}N_{0.40}$	0	59.3 ± 0.7	11.0 ± 0.2	28.3 ± 0.8	1.4 ± 0.1	0.16	0.40
	4	36.3 ± 0.5	11.1 ± 0.8	20.5 ± 0.2	32.1 ± 0.3	0.23	0.43
	8	35.3 ± 0.7	11.1 ± 0.2	18.8 ± 0.3	34.8 ± 0.6	0.24	0.41

Figure 2 shows the grazing-incident XRD patterns of the as-deposited Ta–Zr–N thin films. Although the atomic ratio of N/(Ta + Zr) deviated from the stoichiometric value of 1, the $Ta_{0.81}Zr_{0.19}N_{0.52}$, $Ta_{0.58}Zr_{0.42}N_{0.59}$, and $Ta_{0.33}Zr_{0.67}N_{0.68}$ thin films exhibited a face-centered cubic (fcc) structure. For transition-metal-nitride coatings, N vacancy concentrations can be up to 50% [20]. Matenoglou et al. [21] reported that the ternary transition metal nitrides $Ta_xMe_{1-x}N$ (Me = Ti, Zr, Hf, Nb, Ta, Mo, W) formed solid solutions over the entire x range ($0 < x < 1$) and that they were stable in the rock-salt structure regardless of the valence electron configuration of its constituent metals.

Furthermore, the reflections shift left as Zr content in the Ta–Zr–N thin films increases because the lattice parameters of standard cubic TaN and ZrN are 0.4340 nm (ICDD 49-1283) and 0.4577 nm (ICDD 35-0753), respectively. By contrast, the $Ta_{0.84}Zr_{0.16}N_{0.40}$ thin film exhibited a mixture of hexagonal β-Ta[89-1545], hexagonal γ-Ta_2N (ICDD 26-0985), and cubic ZrN phases, which is attributable to the severe lack of N content in the thin films. Since the standard Gibbs free energies of the metal nitride formation of TaN, Ta_2N, and ZrN at 400 °C are −391,001 J/(mol of N_2), −420,567 J/(mol of N_2), and −602,902 J/(mol of N_2) [22], respectively, ZrN formed preferentially, followed by Ta_2N. The deficiency of N in the $Ta_{0.84}Zr_{0.16}N_{0.40}$ coating resulted in that an excess Ta remained in the β-Ta phase but no N atoms were available to form TaN. The N content of the Ta–Zr–N thin films decreased with increasing power supplied on the Ta target (W_{Ta}), which was attributed to the re-sputtering of N atoms from the surface resulting from the increasing energy of bombarding ions [23,24].

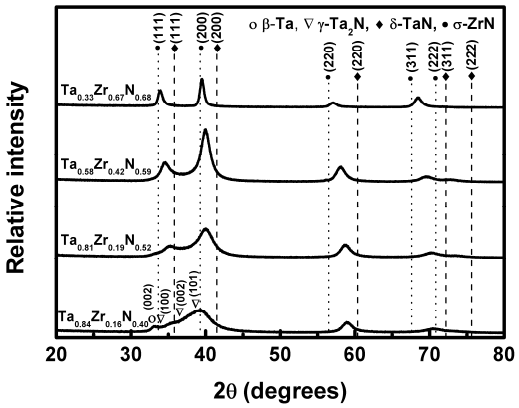

Figure 2. XRD patterns of as-deposited Ta–Zr–N thin films prepared on Si substrates.

Figures 3 and 4 present the AFM and cross-sectional SEM images of the as-deposited Ta–Zr–N thin films, respectively. The $Ta_{0.84}Zr_{0.16}N_{0.40}$, $Ta_{0.81}Zr_{0.19}N_{0.52}$, and $Ta_{0.58}Zr_{0.42}N_{0.59}$ thin films exhibited a smooth surface and a dense structure with a surface roughness of 0.4–0.5 nm (Table 3). By contrast, the $Ta_{0.33}Zr_{0.67}N_{0.68}$ thin film exhibited a coarser columnar structure with a high surface roughness of 2.5 nm. The film structure transition from columnar to dense non-columnar was attributed to the increasing energy of bombarding ions [25,26].

Table 3. Film and oxide scale thicknesses, surface roughness, mechanical properties, elastic recovery, and residual stress values of as-deposited and 600 °C-annealed Ta–Zr–N thin films prepared on Si substrates.

Sample	T_A (h)	Thickness		Surface	H	E	H^3/E^2	W_e	Residual
		Film	Oxide	Roughness					Stress
		(nm)	(nm)	(nm)	(GPa)	(GPa)	(GPa)	%	(GPa)
$Ta_{0.33}Zr_{0.67}N_{0.68}$	0	1217	0	2.54 ± 0.01	30.2 ± 0.9	306 ± 7	0.30	67	−4.18 ± 0.04
	4	1176	0	2.93 ± 0.02	28.3 ± 1.6	283 ± 4	0.28	63	–
	8	979	41	3.55 ± 0.58	19.3 ± 1.6	235 ± 7	0.13	56	–
$Ta_{0.58}Zr_{0.42}N_{0.59}$	0	1238	0	0.52 ± 0.02	35.0 ± 0.6	311 ± 3	0.44	73	−6.17 ± 0.47
	4	1208	62	0.80 ± 0.00	25.7 ± 0.4	262 ± 3	0.25	62	–
	8	1131	151	1.65 ± 0.28	24.8 ± 0.5	268 ± 4	0.21	59	–
$Ta_{0.81}Zr_{0.19}N_{0.52}$	0	1279	0	0.36 ± 0.06	35.5 ± 0.4	299 ± 3	0.50	76	−4.84 ± 0.04
	4	1192	136	1.06 ± 0.10	21.5 ± 0.4	254 ± 6	0.15	56	−3.46 ± 0.19
	8	1149	195	1.40 ± 0.24	19.5 ± 0.3	244 ± 3	0.13	50	−2.80 ± 0.01
$Ta_{0.84}Zr_{0.16}N_{0.40}$	0	1253	0	0.37 ± 0.01	31.9 ± 0.8	258 ± 11	0.49	75	−4.65 ± 0.20
	4	1164	131	0.54 ± 0.02	20.9 ± 0.5	251 ± 3	0.14	56	−2.60 ± 0.17
	8	1071	221	1.15 ± 0.29	18.0 ± 0.3	235 ± 2	0.11	52	−2.80 ± 0.00

Note: T_A: Annealing time.

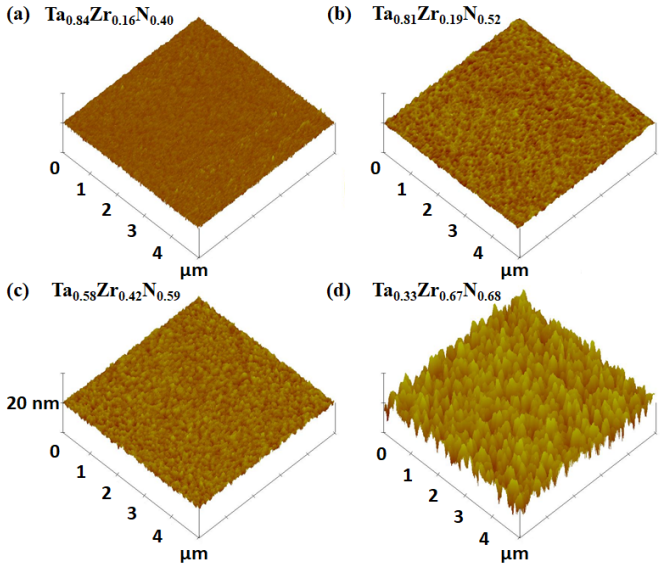

Figure 3. Atomic force microscopy (AFM) images of as-deposited Ta–Zr–N thin films prepared on Si substrates. (**a**) $Ta_{0.84}Zr_{0.16}N_{0.40}$; (**b**) $Ta_{0.81}Zr_{0.19}N_{0.52}$; (**c**) $Ta_{0.58}Zr_{0.42}N_{0.59}$; (**d**) $Ta_{0.33}Zr_{0.67}N_{0.68}$.

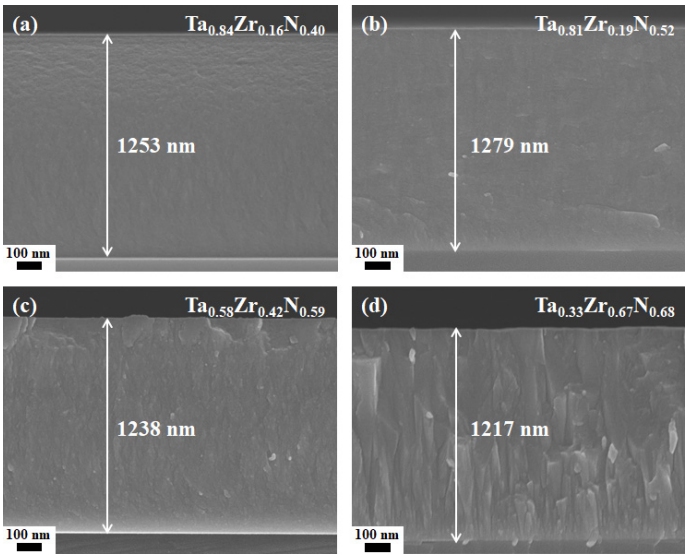

Figure 4. Cross-sectional SEM images of as-deposited Ta–Zr–N thin films prepared on Si substrates. (**a**) $Ta_{0.84}Zr_{0.16}N_{0.40}$; (**b**) $Ta_{0.81}Zr_{0.19}N_{0.52}$; (**c**) $Ta_{0.58}Zr_{0.42}N_{0.59}$; (**d**) $Ta_{0.33}Zr_{0.67}N_{0.68}$.

Table 3 shows the mechanical properties of the as-deposited Ta–Zr–N thin films prepared on Si substrates. The nanoindentation hardness of fcc $Ta_{0.81}Zr_{0.19}N_{0.52}$, $Ta_{0.58}Zr_{0.42}N_{0.59}$, and $Ta_{0.33}Zr_{0.67}N_{0.68}$ thin films were 35.5, 35.0, and 30.2 GPa, respectively, whereas the nanoindentation hardness of the $Ta_{0.84}Zr_{0.16}N_{0.40}$ thin film with mixed phases was 31.9 GPa. The elastic moduli of $Ta_{0.81}Zr_{0.19}N_{0.52}$, $Ta_{0.58}Zr_{0.42}N_{0.59}$, and $Ta_{0.33}Zr_{0.67}N_{0.68}$ thin films were similar (299, 311, and 306 GPa, respectively) because elastic modulus is an intrinsic material property dependent on atomic bonding and crystalline structure [27]. By contrast, the elastic modulus of the $Ta_{0.84}Zr_{0.16}N_{0.40}$ thin film exhibited a lower value of 258 GPa, which was attributed to the implantation of a soft Ta phase. The H^3/E^2 values indicate a resistance to plastic deformation [28], and were 0.49, 0.50, 0.44, and 0.30 for the $Ta_{0.84}Zr_{0.16}N_{0.40}$, $Ta_{0.81}Zr_{0.19}N_{0.52}$, $Ta_{0.58}Zr_{0.42}N_{0.59}$, and $Ta_{0.33}Zr_{0.67}N_{0.68}$ thin films, respectively. The elastic recovery W_e [29] of the as-deposited Ta–Zr–N thin films exhibited a level of 67%–76%. In a previous study using the same sputtering system [30], the HIPIMS-fabricated ZrN_x thin films (x = 0.65–0.78) exhibited

a hardness of 26–27 GPa, a Young's modulus of 260–290 GPa, a residual stress of −4.2–−5.2 GPa, and a surface roughness of approximately 0.5 nm in the as-deposited state. The introduction of Ta into the ZrN-based thin films evidently raised the hardness values and maintained similar Young's modulus levels.

Aouadi [2] reported the mechanical properties of overstoichiometric Ta–Zr–N films deposited by reactive unbalanced magnetron DC sputtering, which exhibited a hardness of <30 GPa with a wide range of Ta/(Ta + Zr) ratios (0.16–0.78) except for the film with a Ta/(Ta + Zr) ratio of 0.29, which exhibited a sudden increased hardness of 37 GPa attributed to solid solution hardening and limited segregation of solutes at grain boundaries. Abadias et al. [4,5] reported a hardness level of ~30 GPa for $Zr_{1-x}Ta_xN$ films (x = 0.51–0.78) prepared using DC magnetron co-sputtering. The residual stress was −4.65, −4.84, −6.17, and −4.18 GPa for the as-deposited $Ta_{0.84}Zr_{0.16}N_{0.40}$, $Ta_{0.81}Zr_{0.19}N_{0.52}$, $Ta_{0.58}Zr_{0.42}N_{0.59}$, and $Ta_{0.33}Zr_{0.67}N_{0.68}$ thin films (Table 3), respectively. These values were more negative than those with similar Zr/(Ta + Zr) ratios reported in our previous study [6], in which the residual stress of the DC-sputtered $Ta_{1-x}Zr_xN_y$ thin films (x = 0.17–0.72, y = 1.03–1.09) ranged from 0 to −2.11 GPa. Residual stress affects the hardness of the coatings; in other words, compressive stress increases coating hardness, whereas tensile stress reduces it [31]. The as-deposited Ta–Zr–N thin films with a wide Zr/(Ta + Zr) ratio range of 0.16–0.67 fabricated in this study exhibited nanoindentation hardnesses of 30–35 GPa, superior to the 22–26 GPa reported for the DC-sputtered $Ta_{0.83}Zr_{0.17}N_{1.03}$, $Ta_{0.59}Zr_{0.41}N_{1.09}$, and $Ta_{0.28}Zr_{0.72}N_{1.05}$ thin films [6].

3.2. Ta–Zr–N Thin Films Annealed in a 15-ppm O_2-N_2 Atmosphere at 600 °C

Table 2 lists the elemental compositions of the Ta–Zr–N thin films annealed at 600 °C in a 15-ppm O_2–N_2 atmosphere for 4 and 8 h. The atomic ratios of Zr/(Ta + Zr) of the annealed $Ta_{0.58}Zr_{0.42}N_{0.59}$ and $Ta_{0.33}Zr_{0.67}N_{0.68}$ thin films retained their values in the as-deposited states (0.42 and 0.67, respectively), whereas the Zr/(Ta + Zr) ratios of the annealed $Ta_{0.84}Zr_{0.16}N_{0.40}$ and $Ta_{0.81}Zr_{0.19}N_{0.52}$ thin films increased from 0.16 to 0.23 and from 0.19 to 0.31, respectively. By contrast, the atomic ratios of Ta:Zr of the DC-sputtered $Ta_{1-x}Zr_xN_y$ thin films (x = 0.05–0.72, y = 0.97–1.05) [6] retained their preannealing values after annealing at 600 °C in 15-ppm O_2-N_2 for 4 h. Moreover, the DC-sputtered $Ta_{1-x}Zr_xN_y$ thin films were near-stoichiometric, whereas the Ta–Zr–N thin films in this study were understoichiometric. Furthermore, the DC-sputtered $Ta_{1-x}Zr_xN_y$ thin films with a higher Zr content gathered a higher O content after annealing, which was in contrast to the Ta–Zr–N thin films prepared in this study. The HIPIMS/RFMS-fabricated Ta–Zr–N thin films with a lower Zr content gathered a higher O content after annealing. These results implied that the variations of Zr/(Ta + Zr) ratio and O content of the annealed Ta–Zr–N thin films in this study were caused by nonstoichiometric compositions, which contributed a high degree of nonmetal site vacancies in the nitride structure; therefore, O quickly diffused inward. Conversely, Zr preferentially diffused outward and reacted with O to form ZrO_2 around the near-surface region because Zr possesses a lower mass than Ta does, and because the standard Gibbs free energies of the metal oxide formations of ZrO_2 and Ta_2O_5 at 600 °C are −931,249 and −663,572 J per mole of oxygen molecules [22], respectively. Since ZrO_2 was the dominant oxide and is not volatile, and the chemical composition analysis was conducted on the surface, the Zr/(Ta + Zr) ratios maintained and increased for the high- and low-Zr-content films, respectively. The N/(Ta + Zr) ratios of the annealed $Ta_{0.81}Zr_{0.19}N_{0.52}$, $Ta_{0.58}Zr_{0.42}N_{0.59}$, and $Ta_{0.33}Zr_{0.67}N_{0.68}$ thin films decreased slightly due to the replacement of N by O in the beginning of oxidation, whereas the N/(Ta + Zr) ratio of the annealed $Ta_{0.84}Zr_{0.16}N_{0.40}$ thin films maintained a level similar to that at the as-deposited state due to the high degree of understoichiometric structure.

The XRD patterns of the 4-h-annealed Ta–Zr–N thin films (data not shown) did not differ from those of the corresponding as-deposited thin films. Figure 5 presents the XRD patterns of the 8-h-annealed Ta–Zr–N thin films, which also exhibited reflections similar to those of the as-deposited thin films except that a wide diffraction reflection appeared at the 2θ angle of approximately 30° for the $Ta_{0.33}Zr_{0.67}N_{0.68}$ thin film, which is attributable to the formation of a surface oxide scale

comprising ZrO_2. The thicknesses of surface oxide scales were 131, 136, 62, and 0 nm and 221, 195, 151, and 41 nm (Figure 6) for the 4- and 8-h-annealed $Ta_{0.84}Zr_{0.16}N_{0.40}$, $Ta_{0.81}Zr_{0.19}N_{0.52}$, $Ta_{0.58}Zr_{0.42}N_{0.59}$, and $Ta_{0.33}Zr_{0.67}N_{0.68}$ thin films, respectively. Figure 7a shows the cross-sectional TEM image of the 8-h-annealed $Ta_{0.58}Zr_{0.42}N_{0.59}$ thin film, whose selected area diffraction pattern exhibits an fcc phase. The high-resolution image (Figure 7b) of the outermost surface region exhibits an amorphous oxide scale of approximately 13 nm. Lattice fringes with d-spacings of 0.224 and 0.259 nm, which respectively correlate to the stacking of (200) and (111) planes, were identified beneath the outermost surface oxide region. The dark-field image corresponding to the (111) diffraction spot in Figure 7a reveals a fine columnar structure with a width of 30 nm (Figure 7c). Figure 8a shows the cross-sectional TEM image of the 8-h-annealed $Ta_{0.33}Zr_{0.67}N_{0.68}$ thin film, whose columnar structure and diffraction pattern are more evident than those of the annealed $Ta_{0.58}Zr_{0.42}N_{0.59}$ thin film. Figure 8b indicates that crystalline ZrO_2 domains were observed in the surface oxide scale of the annealed $Ta_{0.33}Zr_{0.67}N_{0.68}$ thin film. The lattice fringes of (200) and (111) planes in the columnar nitride structure show d-spacings of 0.229 and 0.263 nm, respectively. Figure 8c exhibits the dark-field image corresponding to the (111) diffraction spot in Figure 8a and reveals a coarser columnar width of 95 nm. The oxide scales of $Ta_{0.84}Zr_{0.16}N_{0.40}$ and $Ta_{0.81}Zr_{0.19}N_{0.52}$ were inferred to be amorphous because no oxide reflections were observed in their XRD patterns.

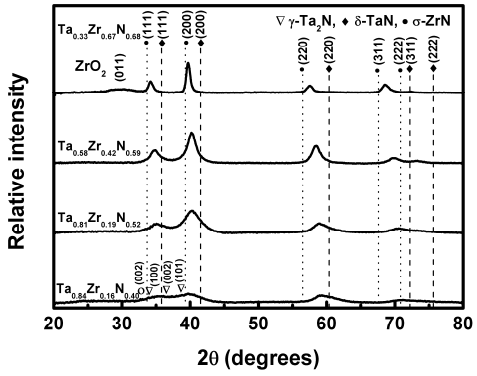

Figure 5. XRD patterns of the Ta–Zr–N thin films after annealing at 600 °C in 15 ppm O_2-N_2 for 8 h.

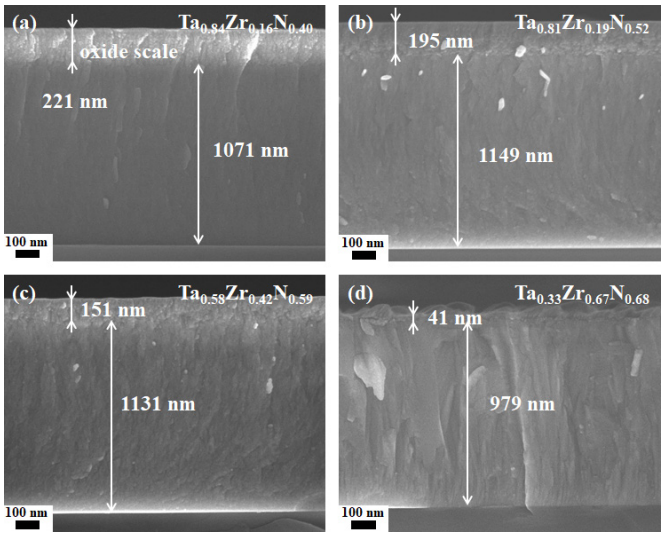

Figure 6. Cross-sectional SEM images of the Ta–Zr–N thin films after annealing at 600 °C in 15 ppm O_2-N_2 for 8 h. (**a**) $Ta_{0.84}Zr_{0.16}N_{0.40}$; (**b**) $Ta_{0.81}Zr_{0.19}N_{0.52}$; (**c**) $Ta_{0.58}Zr_{0.42}N_{0.59}$; (**d**) $Ta_{0.33}Zr_{0.67}N_{0.68}$.

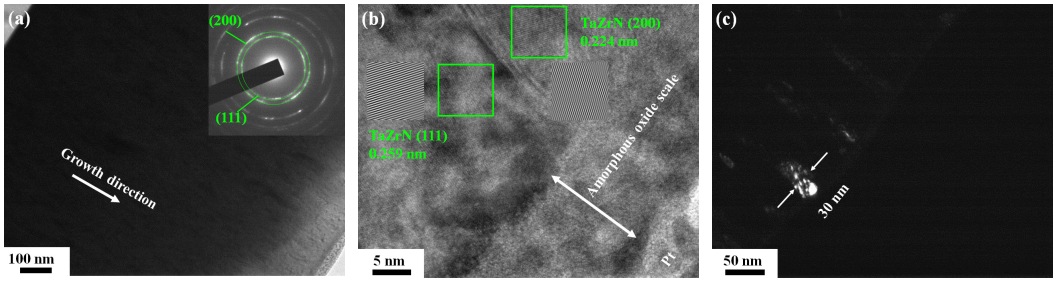

Figure 7. (**a**) Cross-sectional TEM image of the $Ta_{0.58}Zr_{0.42}N_{0.59}$ thin film after annealing at 600 °C in 15 ppm O_2-N_2 for 8 h; (**b**) high-resolution image of the outermost surface region; and (**c**) dark-field image corresponding to the (111) diffraction spot.

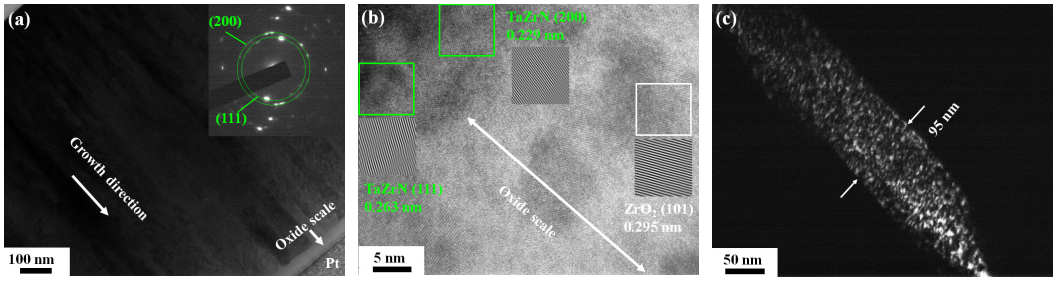

Figure 8. (**a**) Cross-sectional TEM image of the $Ta_{0.33}Zr_{0.67}N_{0.68}$ thin film after annealing at 600 °C in 15 ppm O_2-N_2 for 8 h; (**b**) high-resolution image of the near-surface region; and (**c**) dark-field image corresponding to the (111) diffraction spot.

The vital characteristics of the protective coatings on glass molding dies were high hardness, low surface roughness, and chemical inertness against moldable optical glasses [6,8,32,33]. The formation of amorphous surface oxide scales on high-Ta-content Ta–Zr–N thin films restricted the increase in surface roughness relative to that of crystalline oxide scales formed on high-Zr-content $Ta_{0.33}Zr_{0.67}N_{0.68}$ thin films (Table 3). Since the hardness values of the moldable optical glasses ranged from 3.2 to 7.0 GPa, the protective coatings with a hardness higher than 10 GPa were preferred [8]. Although the hardness measurement of the annealed thin films included the contribution of surface oxide scale, this hardness value implied a realistic strength against the glasses in the molding process. The nanoindentation hardnesses decreased to 20.9, 21.5, 25.7, and 28.3 GPa for the 4-h-annealed $Ta_{0.84}Zr_{0.16}N_{0.40}$, $Ta_{0.81}Zr_{0.19}N_{0.52}$, $Ta_{0.58}Zr_{0.42}N_{0.59}$, and $Ta_{0.33}Zr_{0.67}N_{0.68}$ thin films (Table 3), respectively; furthermore, the nanoindentation hardnesses decreased to 18.0, 19.5, 24.8, and 19.3 GPa after 8 h of annealing, respectively. Both the H^3/E^2 ratio and elastic recovery W_e exhibited decreased trends with increasing the annealing time due to the formation of surface oxide. The residual stress of annealed $Ta_{0.84}Zr_{0.16}N_{0.40}$ and $Ta_{0.81}Zr_{0.19}N_{0.52}$ thin films decreased to a range of −2.6 to −3.5 GPa (Table 3). The annealed $Ta_{0.58}Zr_{0.42}N_{0.59}$ and $Ta_{0.33}Zr_{0.67}N_{0.68}$ thin films exhibited local detachment after annealing; hence, the residual stress could not be evaluated. In a previous study [30], the nanoindentation hardness values of the HIPIMS-fabricated ZrN_x thin films declined from 26–27 GPa to less than 10 GPa after they were annealed at 600 °C in 15 ppm O_2–N_2 for 2 h owing to the formation of crystalline ZrO_2 scales, which was accompanied by an increase in the surface roughness from 0.5 to 3–6 nm.

4. Conclusions

We reported the preparation of understoichiometric Ta–Zr–N thin films with atomic ratios (N/(Ta + Zr)) of 0.40–0.68 through HIPIMS/RFMS co-sputtering. The as-deposited high-Ta-content Ta–Zr–N thin films $Ta_{0.84}Zr_{0.16}N_{0.40}$, $Ta_{0.81}Zr_{0.19}N_{0.52}$, and $Ta_{0.58}Zr_{0.42}N_{0.59}$ exhibited nanoindentation hardnesses of 32–35 GPa, Young's moduli of 258–311 GPa, H^3/E^2 values of 0.44–0.50 GPa,

elastic recovery of 73%–76%, and surface roughnesses of 0.4–0.5 nm. The HIPIMS technique helps to fabricate dense and smooth thin films. After annealing at 600 °C in a 15-ppm O_2-N_2 atmosphere for 4 h, the nanoindentation hardnesses decreased to 21–26 GPa and the surface roughnesses increased to 0.5–1.1 nm. The nanoindentation hardnesses further decreased to 18–25 GPa and the surface roughnesses further increased to 1.2–1.6 nm after 8 h of annealing. The introduction of Ta into the HIPIMS-fabricated ZrN thin films evidently raised the hardness values in the as-deposited state and varied the oxide scale to be a ZrO_2-dominant amorphous layer after annealing; the amorphous layer decreased the oxidation rate and reduced the declining trend of the hardness during annealing. Amorphous surface oxide scales restricted an increase in surface roughness. The HIPIMS/RFMS-co-sputtered Ta–Zr–N thin films exhibited a nanoindentation hardness of 30–35 GPa with a Zr/(Ta + Zr) ratio range of 0.16–0.67; this range was wider than those of the conventional DC-sputtered Ta–Zr–N thin films with a hardness >30 GPa.

Acknowledgments: The financial supports of this work from the Ministry of Science and Technology, Taiwan, under contract nos. 104-2622-E-131-005 and 105-2221-E-131-004 are appreciated.

Author Contributions: Li-Chun Chang designed the experiments and wrote the paper; Ching-Yen Chang performed the experiments; and Ya-Wen You analyzed the TEM data.

Conflicts of Interest: The authors declare no conflict of interest. The founding sponsors had no role in the design of the study; in the collection, analyses, or interpretation of data; in the writing of the manuscript; or in the decision to publish the results.

References

1. Aouadi, S.M.; Filip, P.; Debessai, M. Characterization of tantalum zirconium nitride sputter-deposited nanocrystalline coatings. *Surf. Coat. Technol.* **2004**, *187*, 177–184. [CrossRef]
2. Aouadi, S.M. Structural and mechanical properties of TaZrN films: Experimental and ab initio studies. *J. Appl. Phys.* **2006**, *99*, 053507. [CrossRef]
3. Ruan, J.L.; Huang, J.L.; Lu, H.H.; Chen, J.S.; Lii, D.F. Effects of the Ta content on the microstructure and electrical property of reactively sputtered $Ta_xZr_{1-x}N$ thin films. *Thin Solid Films* **2011**, *519*, 4987–4991. [CrossRef]
4. Abadias, G.; Kanoun, M.B.; Goumri-Said, S.; Koutsokeras, L.; Dub, S.N.; Djemia, P. Electronic structure and mechanical properties of ternary ZrTaN alloys studied by ab initio calculations and thin-film growth experiments. *Phys. Rev. B* **2014**, *90*, 114107. [CrossRef]
5. Abadias, G.; Djemia, P.; Belliard, L. Alloying effects on the structure and elastic properties of hard coatings based on ternary transition metal (*M* = Ti, Zr or Ta) nitrides. *Surf. Coat. Technol.* **2014**, *257*, 129–137. [CrossRef]
6. Chang, L.C.; Chang, C.Y.; Chen, Y.I. Mechanical properties and oxidation resistance of reactively sputtered $Ta_{1-x}Zr_xN_y$ thin films. *Surf. Coat. Technol.* **2015**, *280*, 27–36. [CrossRef]
7. Liu, S.C.; Chen, Y.I.; Tsai, H.Y.; Lin, K.C.; Chen, Y.H. Thermal stability of Ir–Re coatings annealed in oxygen-containing atmospheres. *Surf. Coat. Technol.* **2013**, *237*, 105–111. [CrossRef]
8. Liu, S.C.; Chen, Y.I.; Shyu, J.J.; Tsai, H.Y.; Lin, K.Y.; Chen, Y.H.; Lin, K.C. The chemical inertness of Ir–Re and Ta–Ru coatings in molding B_2O_3–ZnO–La_2O_3-based glass. *Surf. Coat. Technol.* **2014**, *259*, 352–357. [CrossRef]
9. Kouznetsov, V.; Macák, K.; Schneider, J.M.; Helmersson, U.; Petrov, I. Functional differences between the external and protoplasmic surfaces of plasma membranes in activating vaccinia virus infectivity. *Surf. Coat. Technol.* **1990**, *122*, 290–293. [CrossRef]
10. Helmersson, U.; Lattemann, M.; Bohlmark, J.; Ehiasarian, A.P.; Gudmundsson, J.T. Ionized physical vapor deposition (IPVD): A review of technology and applications. *Thin Solid Films* **2006**, *513*, 1–24. [CrossRef]
11. Purandare, Y.P.; Ehiasarian, A.P.; Hovsepian, P.E. Structure and properties of ZrN coatings deposited by high power impulse magnetron sputtering technology. *J. Vac. Sci. Technol. A* **2011**, *29*, 011004. [CrossRef]
12. Schmidt, S.; Czigány, Z.; Greczynski, G.; Jensen, J.; Hultman, L. Influence of inert gases on the reactive high power pulsed magnetron sputtering process of carbon-nitride thin films. *J. Vac. Sci. Technol. A* **2013**, *31*, 011503. [CrossRef]

13. Magnus, F.; Ingason, A.S.; Olafsson, S.; Gudmundsson, J.T. Nucleation and resistivity of ultrathin TiN films grown by high-power impulse magnetron sputtering. *IEEE Electron. Dev. Lett.* **2012**, *33*, 1045–1047. [CrossRef]
14. Alami, J.; Sarakinos, K.; Mark, G.; Wuttig, M. On the deposition rate in a high power pulsed magnetron sputtering discharge. *Appl. Phys. Lett.* **2006**, *89*, 154104. [CrossRef]
15. Greczynski, G.; Lu, J.; Jensen, J.; Bolz, S.; Kölker, W.; Schiffers, C.; Lemmer, O.; Greene, J.E.; Hultman, L. A review of metal-ion-flux-controlled growth of metastable TiAlN by HIPIMS/DCMS Co-sputtering. *Surf. Coat. Technol.* **2014**, *257*, 15–25. [CrossRef]
16. Ding, J.; Zhang, T.; Yun, J.M.; Kang, M.C.; Wang, Q.; Kim, K.H. Microstructure, mechanical, oxidation and corrosion properties of the Cr-Al-Si-N coatings deposited by a hybrid sputtering system. *Coatings* **2017**, *7*, 119. [CrossRef]
17. Oliver, W.C.; Pharr, G.M. An improved technique for determining hardness and elastic modulus using load and displacement sensing indentation experiments. *J. Mater. Res.* **1992**, *7*, 1564–1583. [CrossRef]
18. Simmons, G.; Wang, H. *Single Crystal Young's Constants and Calculated Aggregate Properties: A Handbook*; MIT Press: Cambridge, MA, USA, 1971.
19. Janssen, G.C.A.M.; Abdalla, M.M.; van Keulen, F.; Pujada, B.R.; van Venrooy, B. Celebrating the 100th anniversary of the Stoney equation for film stress: Developments from polycrystalline steel strips to single crystal silicon wafers. *Thin Solid Films* **2009**, *517*, 1858–1867. [CrossRef]
20. Thod, L.E. *Transition Metal Carbides and Nitrides*; Academic Press: New York, NY, USA, 1971.
21. Matenoglou, G.M.; Koutsokeras, L.E.; Lekka, C.E.; Abadias, G.; Kosmidis, C.; Evangelakis, G.A.; Patsalas, P. Structure, stability and bonding of ternary transition metal nitrides. *Surf. Coat. Technol.* **2009**, *204*, 911–914. [CrossRef]
22. Barin, I. *Thermochemical Data of Pure Substances*, 3rd ed.; VCH: New York, NY, USA, 1995.
23. Hurkmans, T.; Lewis, D.B.; Paritong, H.; Brooks, J.S.; Münz, W.D. Influence of ion bombardment on structure and properties of unbalanced magnetron grown CrN_x coatings. *Surf. Coat. Technol.* **1999**, *114*, 52–59. [CrossRef]
24. Musil, J.; Šícha, J.; Heřman, D.; Čerstvý, R. Role of energy in low-temperature high-rate formation of hydrophilic TiO_2 thin films using pulsed magnetron sputtering. *J. Vac. Sci. Technol. A* **2007**, *25*, 666–674. [CrossRef]
25. Musil, J. Hard nanocomposite coatings: Thermal stability, oxidation resistance and toughness. *Surf. Coat. Technol.* **2012**, *207*, 50–65. [CrossRef]
26. Musil, J.; Jaroš, M.; Čerstvý, R.; Haviar, S. Evolution of microstructure and macrostress in sputtered hard Ti(Al,V)N films with increasing energy delivered during their growth by bombarding ions. *J. Vac. Sci. Technol. A* **2017**, *35*, 020601. [CrossRef]
27. Zhou, Y.L.; Niinomi, M.; Akahori, T. Changes in mechanical properties of Ti alloys in relation to alloying additions of Ta and Hf. *Mater. Sci. Eng. A* **2008**, *483–484*, 153–156. [CrossRef]
28. Tsui, T.Y.; Pharr, G.M.; Oliver, W.C.; Bhatia, C.S.; White, R.L.; Anders, S.; Anders, A.; Brown, I.G. Nanoindentation and nanoscratching of hard carbon coatings for magnetic disks. *Mater. Res. Soc. Symp. Proc.* **1995**, *383*, 447–452. [CrossRef]
29. Musil, J.; Kunc, F.; Zeman, H.; Poláková, H. Relationships between hardness, Young's modulus and elastic recovery in hard nanocomposite coatings. *Surf. Coat. Technol.* **2002**, *154*, 304–313. [CrossRef]
30. Chang, L.C.; Chang, C.Y.; Chen, Y.I.; Kao, H.L. Mechanical properties and oxidation behavior of ZrN_x thin films fabricated through high-power impulse magnetron sputtering deposition. *J. Vac. Sci. Technol. A* **2016**, *34*, 02D107. [CrossRef]
31. Bielawski, M. Residual stress control in TiN/Si coatings deposited by unbalanced magnetron sputtering. *Surf. Coat. Technol.* **2006**, *200*, 3987–3995. [CrossRef]
32. Chen, Y.I.; Wang, H.H. Oxidation resistance and mechanical properties of Cr–Ta–Si–N coatings in glass molding processes. *Surf. Coat. Technol.* **2014**, *260*, 118–125. [CrossRef]
33. Chen, Y.I.; Cheng, Y.R.; Chang, L.C.; Lu, T.S. Chemical inertness of Ta–Si–N coatings in glass molding. *Thin Solid Films* **2015**, *584*, 66–71. [CrossRef]